Applied Catalysis B: Environmental 162 (2015) 282–288

Contents lists available at ScienceDirect

Applied Catalysis B: Environmental

journal homepage: www.elsevier.com/locate/apcatb

Self-sustained combustion of carbon monoxide promoted by the Cu-Ce/ZSM-5 catalyst in $CO/O_2/N_2$ atmosphere

Feng Bin [a,*], Xiaolin Wei [a], Bo Li [a], Kwan San Hui [b,**]

[a] State Key Laboratory of High-Temperature Gas Dynamics, Institute of Mechanics, Chinese Academy of Science, Beijing, PR China
[b] Department of Mechanical Convergence Engineering, Hanyang University, 17 Haengdang-dong, Seongdong-gu, Seoul 133-791, Republic of Korea

ARTICLE INFO

Article history:
Received 4 May 2014
Received in revised form 28 June 2014
Accepted 2 July 2014
Available online 9 July 2014

Keywords:
Carbon monoxide
Self-sustained combustion
Cu-Ce/ZSM-5
Catalytic activity

ABSTRACT

The Cu/ZSM-5, Ce/ZSM-5 and Cu-Ce/ZSM-5 catalysts were prepared and characterized in this investigation and the catalytic activity of carbon monoxide (CO) combustion under these catalysts was determined by temperature-programmed oxidation. The activity for the CO combustion follows the decreasing order: Cu-Ce/ZSM-5 > Cu/ZSM-5 > Ce/ZSM-5, indicated by lower ignition, light-off, extinction temperature and broader hysteresis determined via both heating and cooling feeding process. The CO adsorbed on the copper sites to form Cu^+–CO complexes, monodentate and bidentate carbonates was considered to be the crucial step for CO catalytic combustion. At the CO concentration ≥5 vol.%, the CO self-sustained combustion was achieved over the Cu-Ce/ZSM-5 catalyst. One reason is due to formation of Cu^{2+} ions incorporated into cerium oxides, which are more reducible than the copper clusters, minicrystals and bulk CuO particles. Another reason is attributable to the formation of Ce^{4+}/Ce^{3+} redox couple, which facilitates oxygen transport on the catalyst surface.

1. Introduction

The off-gas produced during steelmaking is generally used as fuels in the rolling plant. This off-gas contains approximate 70 vol.% of carbon monoxide (CO), and thus has a heating value of about 9 MJ/Nm^3 [1]. However, the CO concentration periodically varies along with the tap-to-tap cycle, and decreases down to 20 vol.% below at the start and end of steelmaking. In this case, because high concentration of oxygen together with CO is liable to cause explosions, the off-gas generated at these moments is not recovered directly, but often discharges into the atmosphere via conventional flare burners [2].

Catalytic postcombustion allows oxidizing CO to CO_2 at low temperatures, and thereby is considered as an effective strategy to produce heat suitable for electric power generation [3,4]. Our new scenario related to the device miniaturization is identified recently, starting from the so-called "methane self-sustained catalytic combustion". In this process, the $CH_4 + O_2$ mixture is firstly catalyzed to generate local high-temperature spots on the catalyst surface. These hot spots then dissociate adjacent CH_4 and O_2 molecules, leading to a thermo-chemical runaway followed by rapid transitions to a self-sustained intense burning [5]. If the self-sustained catalytic combustion can be achieved during the $CO \rightarrow CO_2$ oxidation, one advantage of this method is the low cost, due to its high combustion efficiency in small-scale devices. Another important advantage is that only a relatively small energy is required for ignition while the high temperatures during the process are generated by the release of reaction heat without external energy required. In recent years, considerable efforts have been devoted to optimize the structure of combustors, heat recirculation system and fuel/oxygen ratio, etc., in order to widening the operating window of self-sustained operation [6–8]. Nevertheless, the research focusing on the catalytic mechanism of CO self-sustained combustion is seldom performed.

The ZSM-5 zeolite is crystalline aluminosilicates with a 3-dimensional, open anion framework consisting of oxygen-sharing SiO_4 and AlO_4 tetrahedra. When transition metals are loaded on the ZSM-5 support, different species are present on the ZSM-5 support as isolated ions, metal oxide clusters, nano-size and large metal oxide particles [9]. Our interest in CO oxidation catalysts has concentrated on copper/cerium-based ZSM-5 zeolites owing to their high activity and thermal stability. Copper oxide is reducible, which depends on the copper existing in various oxidation states [10]. Ceria acts as an oxygen reservoir regulating the partial pressure of oxygen near the catalyst surface and accelerate oxygen transfers

* Corresponding author. Tel.: +86 10 82544222; fax: +86 10 82544222.
** Corresponding author. Tel.: +82 2 22200441; fax: +82 2 22202299.
E-mail addresses: binfeng@imech.ac.cn (F. Bin), kshui@hanyang.ac.kr (K.S. Hui).

http://dx.doi.org/10.1016/j.apcatb.2014.07.007
0926-3373/

[11]. The object of this study is to explore catalytic mechanism of CO self-sustained combustion on basis of the Cu-Ce/ZSM-5 catalyst. The obtained results provide an estimation to prepare catalysts that retain heat released from exothermic reactions so as to obtain a self-sustained combustion at low temperatures, and are also helpful to accept the self-sustained combustion technology of CO in steelmaking off-gas.

2. Experimental specifications

2.1. Synthesis of catalysts

The Cu/ZSM-5 (Cu-Z), Ce/ZSM-5 (Ce-Z) and Cu-Ce/ZSM-5 (CuCe-Z) catalysts, containing 2.0 wt.% copper and/or 2.0 wt.% cerium, were prepared by wet impregnation method. An appropriate amount of copper and cerium nitrates were dissolved in deionized water and mixed with 5 g of commercial H/ZSM-5 (atomic Si/Al ratio = 25, crystallinity = 100%, thermal stability = 1200 °C). The resulting solution was stirred at 80 °C for 24 h, at a pH of about 7.0. After being dried by evaporation, the sample was calcined at 600 °C for 4 h. The copper and cerium concentrations of each catalyst after calcination were determined by atomic absorption in a PerkinElmer AAnalyst 300 spectrometer (AAS).

2.2. Characterization

Nitrogen sorption was measured with a NOVA 2000 gas sorption analyzer at liquid nitrogen temperature (−196 °C). Prior to measurement, each sample was degassed under vacuum for 8 h at 300 °C. The crystalline phase was determined by powder XRD using a Rigaku D/MAC/max 2500 v/pc instrument with Cu Kα radiation (40 kV, 200 mA, $\lambda = 1.5418$ Å). Diffractometer data were acquired with a step size of 0.02° for 2θ values from 5 to 80°. X-ray photoelectron spectra (XPS) were recorded on a Kratos Axis Ultra DLD spectrometer with a monochromated Al-Ka X-ray source and delay line detector. Ultraviolet−visible diffuse reflectance spectra (UV−vis) were measured on a Hitachi U-4100 spectrophotometer with an integration sphere diffuse reflectance attachment. The temperature-programmed reduction with hydrogen (H_2-TPR) experiments were carried out on a Micromeritics 2920 II analyzer with 5 vol.% H_2/Ar at a heating rate of 10 °C/min and a final temperature of 600 °C. Prior to reduction, the sample (*ca.*100 mg) was pretreated in flowing He at 300 °C for 1 h. Oxygen (OSC) and carbon monoxide storage capacity (CSC) measurements were also carried out on the Micromeritics Autochem 2920 II analyzer. The sample (*ca.*100 mg) was reduced at 550 °C for 1 h in 5 vol.% H_2/Ar, then cooled down to 200 °C and purged continuously with He for 20 min. A pulse of oxygen (or carbon monoxide) was injected into the sample until no oxygen (or carbon monoxide) consumption could be detected by TCD. Total OSC (or CSC) was calculated by integrating the oxygen (or carbon monoxide) consumed. In-situ diffuse reflectance Fourier transform (DRIFT) spectra were recorded on the Bruker Tensor 27 spectrometer. The samples (*ca.* 50 mg) were placed in the DRIFT cell. Prior to experiment, the sample was pretreated in He at 300 °C for 1 h, and cooled to the desired temperature for taking a reference spectrum. Then, the reaction gas mixture (2.5 vol.% CO, 20 vol.% O_2, He balance) was fed to the sample at a total flow rate of 30 mL min^{-1}. For each temperature step, a series of time-dependent DRIFT spectra of reaction on the sample were sequentially recorded with a resolution of 4 cm^{-1} and an accumulation of 64 scans.

2.3. Catalytic activity testing

Catalytic experiments were performed at atmospheric pressure in a flow-type apparatus designed for continuous operation. After pressed and sieved into 20–40 meshes, 0.5 g catalyst was packed into a fixed-bed reactor made of a quartz tube with an internal diameter of 8 mm. Two K-type thermocouples were used: The first thermocouple was immersed inside the center of catalyst bed to measure the temperature continuously; the second thermocouple was located between the reactor wall and the oven wall, and was used to control the oven temperature. During each temperature-programmed oxidation (TPO) run, the heating/cooling rate was set at 5 °C/min. The feed gas contained 1 vol.%, 3 vol.% or 5 vol.% CO, 20 vol.% O_2 and N_2 as balance at space velocity of 30,000 h^{-1}. An online FTIR measurement system (QGS-08, Maihak) was used to monitor the effluent CO, O_2 and CO_2. Good reproducibility of catalysts was found for each TPO experiment at five times.

Table 1
Ignition, light-off and extinction temperatures of carbon monoxide catalytic combustion.

CO concentration	Cu-Z (°C)				CuCe-Z (°C)			
	T_i	T_{lo}	T_{ex}	ΔT	T_i	T_{lo}	T_{ex}	ΔT
1%	267	279	273	6	229	235	189	46
3%	243	249	222	27	194	198	126	72
5%	222	227	164	63	180	189	<30	>159

3. Results and discussion

3.1. TPO process of carbon monoxide

Fig. 1 shows the CO conversion over Cu-Z, Ce-Z and CuCe-Z catalysts under heating and cooling feeding conditions. When the concentration of CO is set at 1 vol.%, 3 vol.% and 5 vol.%, the Ce-Z catalyst is inactive for the CO combustion in the temperature range of 50–300 °C. By contrast, the Cu-Z and CuCe-Z catalysts exhibit excellent activities for the CO conversion, which follow three main steps under the heating feed condition. Take the CuCe-Z catalyst at 1 vol.% CO for example (Fig. 1A), the first step can be described as a slow induction process that begins at 177 °C and then continues, at a relatively slow rate until 229 °C. Here the reaction is kinetically controlled, as reflected by the temperature of catalyst bed close to the controlled temperature. The second step includes both the catalytic ignition and light-off processes, where the reaction rate is controlled by internal diffusion in the porous ZSM-5 material, rather than kinetic regime [12]. The catalytic ignition occurs at temperatures (T_{ig}) corresponding to CO conversions below 30%, and takes place at gas–solid phase interface, probably decided by the transfer rate of oxygen [13]. When the oxidation rate is fast enough to induce a strong increase of the local temperature, ignition occurs and then the catalytic light-off phenomenon propagates, allowing the thermal CO combustion. Herein, the light-off temperature is defined as the temperature (T_{lo}) for which 50% CO conversion is achieved. The third phase concerns temperatures well above the light-off region. The rate of heat generation by the CO combustion is much higher than that of heat dissipation, thus leading to a remarkable runaway. Entering this step means the reaction rate becomes controlled by external diffusion [14].

Upon the cooling feeding, the experiment follows a reverse transition from the third to the first step. It is interesting to see that the cooling lines of CO conversions shift toward low temperatures, compared with the heating ones. The hysteresis formed may result from the local heating due to exothermic effect of the oxidation reaction so that the controlled temperature can be decreased below the ignition temperature without influencing the reaction rate significantly. The temperatures related to the CO combustion over Cu-Z and CuCe-Z catalysts are listed in Table 1. The extinction temperature (T_{ex}) is defined as the temperature for which 50% CO conversion is achieved under the cooling feeding condition, and

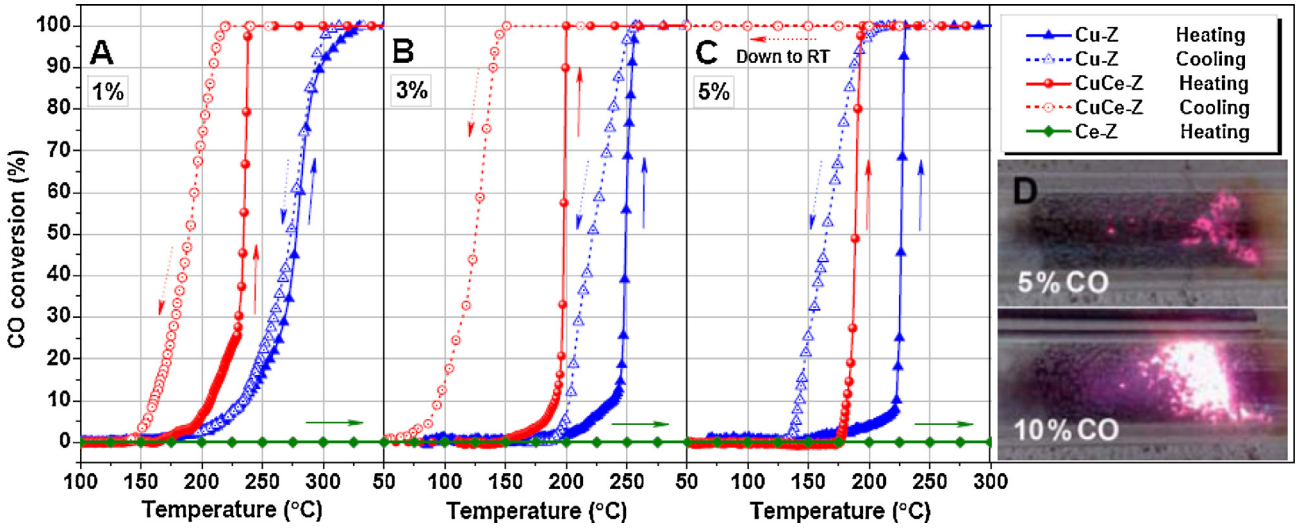

Fig. 1. Temperature-programmed oxidation of 1 vol.% (A), 3 vol.% (B) and 5 vol.% (C) CO with 20 vol.% O_2/He over the Cu-Z, Ce-Z and CuCe-Z catalysts. The inset picture (D) describes the CO self-sustained combustion promoted by the CuCe-Z catalyst (5 vol.% and 10 vol.% CO). The standard deviations for the CO oxidation are within the range of 2.0–3.1.

the temperature interval $\Delta T = T_{lo} - T_{ex}$. As shown, the CuCe-Z catalyst performs much better than the Cu-Z, which is decided by the T_i and T_{lo} values of the CuCe-Z lower than those of the Cu-Z under the same CO concentration. As the CO concentration increasing, the induction process (the first step) of the heating lines is becoming ever shorter for both the Cu-Z and CuCe-Z catalysts, indicating the enhancement of reaction rate. However, significant broadening of hysteresis can be observed for the CuCe-Z catalyst with the CO concentration increasing from 1 vol.% to 3 vol.%, corresponding to the ΔT value increasing from 46 to 72 °C. When the CO concentration is set at 5 vol.%, the CO conversion over the CuCe-Z catalyst attains 100% at 189 °C (Fig. 1C). From that reaction rate, the furnace temperature is then allowed to descend. The most striking observation is that the CO conversion can be consistently maintained even after the heating is stopped and the controlled temperature keeps at a room temperature around 30 °C. It is evident that the fast mass and heat transfer on the gas–solid phase interface promotes this self-sustained combustion. Typical photographs of CO self-sustained combustion are shown in Fig. 1D, and the light intensifies with the increase of CO concentration. The self-sustained combustion of CO under the CuCe-Z catalyst can be maintained for five hours with no deactivation of the catalyst.

3.2. Structure and morphology

The Cu-Z, Ce-Z and CuCe-Z catalysts, together with the ZSM-5 support, were characterized by N_2 sorption measurements. Table 2 shows that doping ZSM-5 with copper and/or cerium leads to a decrease in BET surface area and micropore volume. The reason for this may be that copper and cerium species cover the external surface of ZSM-5, blocking a number of zeolite channels, and impeding entry of N_2 into the pores. XRD patterns (Fig. 2) of pure ZSM-5 and samples doped with copper and/or cerium are characterized by peaks at $2\theta = 7.9°$, 8.8°, 23.1° and 23.8°, which represent the (0 1 1), (2 0 0), (0 5 1) and (3 0 3) planes of their crystal structures, respectively. The intensities of the principal diffraction peaks of ZSM-5 decrease remarkably after the copper and/or cerium introduction. No diffraction peaks attributed to either copper or cerium oxides are observed, which suggests that the copper and cerium species are well dispersed on the ZSM-5 support [15,16].

Table 2
BET surface area and micropore volume of pure ZSM-5, Cu-Z, Ce-Z and CuCe-Z catalysts.

Sample	BET surface area ($m^2\ g^{-1}$)	Micropore volume ($cm^3\ g^{-1}$)
Pure ZSM-5	376	0.15
Cu-Z	362	0.14
Ce-Z	358	0.13
CuCe-Z	317	0.10

3.3. XPS analysis

The chemical states and surface compositions of the elements in the catalysts were characterized by XPS. The Cu 2p spectra of the Cu-Z and CuCe-Z catalysts shows two main peaks in Fig. 3A: a

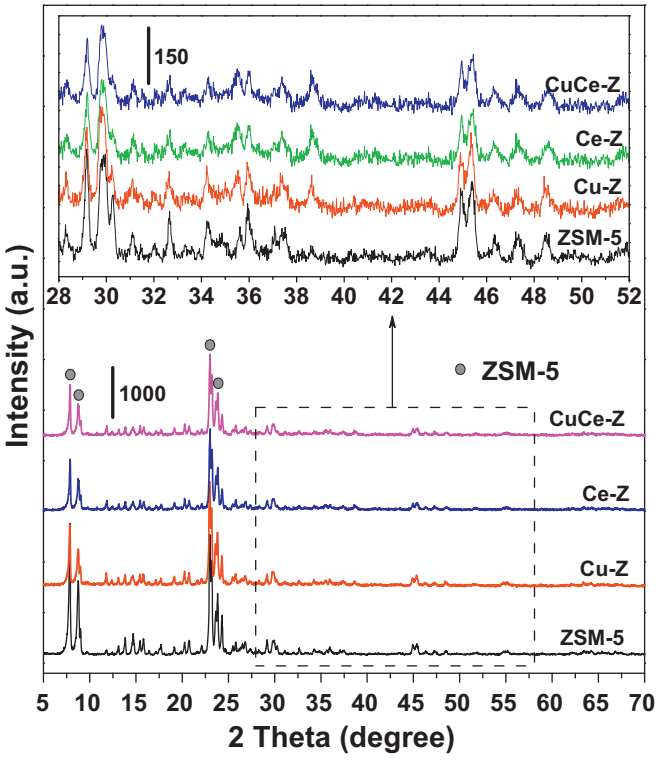

Fig. 2. Wide-angle XRD patterns of pure ZSM-5, Cu-Z and CuCe-Z catalysts after calcination in air at 600 °C for 4 h.

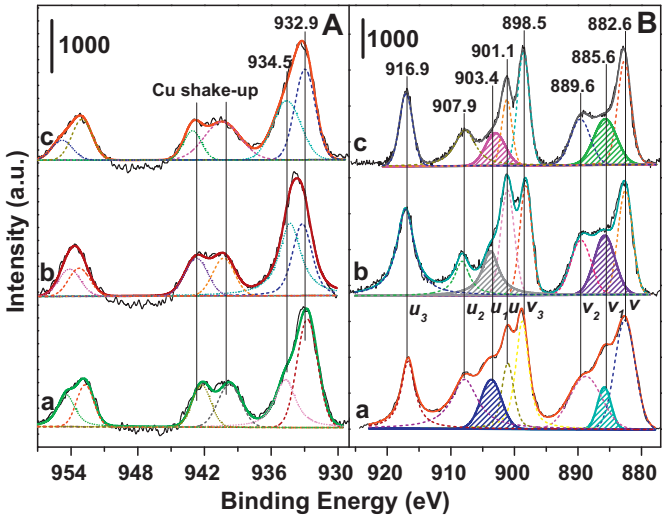

Fig. 3. XPS narrow spectra Cu 2p (A) over the fresh Cu-Z (A, a), fresh CuCe-Z (A, b), used CuCe-Z (A, c) and the spectra Ce 3d (B) over the fresh Ce-Z (B, a), fresh CuCe-Z (B, b) and used CuCe-Z (B, c) catalysts. Crude line: original data; Smooth line: fitting data.

peak at approximately 933 eV that can be attributed to Cu $2p_{3/2}$, and a peak at about 953 eV that can be attributed to Cu $2p_{1/2}$. The intense satellite peaks located in the range of 937.6–945.4 eV confirm the existence of divalent copper. Peak deconvolution and fitting to experimental data indicate that the Cu $2p_{3/2}$ peak can be well fitted by two peaks at 932.9 and 934.5 eV, corresponding to the Cu^+ and Cu^{2+} ions, respectively [17].

Fig. 3B displays the Ce 3d XPS spectra of the Ce-Z and CuCe-Z catalysts, which can be deconvoluted into $3d_{5/2}$ and $3d_{3/2}$ spin–orbit components (labeled as v and u, respectively) describing the $Ce^{4+} \leftrightarrow Ce^{3+}$ electronic transitions. The four intense components v (882.6 eV), u (901.1 eV), v_3 (898.5 eV), u_3 (916.9 eV) as well as the two weaker components v_2 (889.6 eV) and u_2 (907.9 eV) can be attributed to different Ce 4f electron configuration in the final states of the Ce^{4+} species. The v_1 (885.6 eV) and u_1 (903.4 eV) components corresponds to one of the two possible electron configurations of the final state of the Ce^{3+} species [18]. The relative percentage of the Ce^{3+} species is obtained by the areas of the Ce 3d components relative to Ce^{4+} (v, v_2, v_3, u, u_2, u_3) and to Ce^{3+} (v_1, u_1).

The Cu^{2+}/Cu_{total}, Ce^{3+}/Ce_{total}, Cu/Si and Ce/Si surface atomic ratios calculated according to relative peak areas of XPS spectra are listed in Table 3. The Cu/Si and Ce/Si ratios detected by XPS are higher than the bulk (listed in the bracket), indicating that the copper and cerium are enriched on the surface of ZSM-5 grains. The copper is mostly in a univalent oxidation state over Cu-Z. When the cerium is introduced into Cu-Z, the increase of Cu^{2+}/Cu_{total} ratio from 0.403 to 0.562 confirms that part of the Cu^+ is oxidized into Cu^{2+}. It is worth noting, in Table 3, that the Ce^{3+} contribution increases from 0.135 to 0.219 in CuCe-Z as compared with Ce-Z. The presence of Ce^{3+} implies the defect structure of ceria due to oxygen vacancies [19]. The generation of Cu^{2+} together with observation of Ce^{3+} species is indicative of the redox equilibrium

Table 3
Surface atomic ratios of Cu-Z, Ce-Z and CuCe-Z catalysts obtained from XPS analysis. The bulk atomic ratios detected by AAS are listed in the bracket.

Sample	Cu^{2+}/Cu_{total}	Ce^{3+}/Ce_{total}	Cu/Si	Ce/Si
Cu-Z	0.403	/	0.042 (0.013)	0
Ce-Z	/	0.135	0	0.020 (0.006)
CuCe-Z (fresh)	0.562	0.219	0.045 (0.013)	0.018 (0.006)
CuCe-Z (used)	0.472	0.208	0.041 (0.013)	0.017 (0.006)

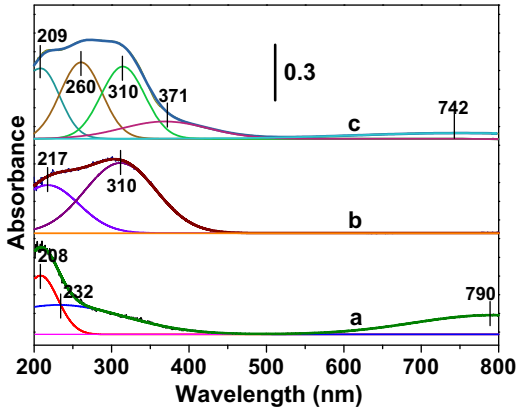

Fig. 4. UV–vis spectra of Cu-Z (a), Ce-Z (b) and CuCe-Z (c) catalysts.

($Cu^+ + Ce^{4+} \leftrightarrow Cu^{2+} + Ce^{3+}$) shifting to right for the CuCe-Z catalyst. After the CO oxidation reaction, the Cu^{2+}/Cu_{total} and Ce^{3+}/Ce_{total} ratio decreases slightly, which in this case follows the equilibrium shifting to left. These results confirm that both copper and cerium participate in CO oxidation reaction.

3.4. UV–vis analysis

UV–vis spectroscopy is applied to understand the nature and coordination of copper oxide species in the samples. As shown in Fig. 4, the Cu-Z catalyst displays two absorption bands at 208 and 232 nm, and a broad band at 790 nm. The absorption band at 208 nm can be assigned to $O^{2-} \rightarrow Cu^+/Cu^{2+}$ charge transfers. The band centered at 232 nm corresponds to the transitions of Cu^{2+} in tetragonal oxygen configuration, which can be assigned to the formation of well dispersed copper clusters on the surface of ZSM-5 grains. The absorption band at 790 nm is related with the transitions of Cu^{2+} in octahedral oxygen configuration more or less tetragonally distorted, corresponding to the CuO phase [20]. The Ce-Z catalyst shows two characteristic peaks at 217 and 310 nm, assigned to $O^{2-} \rightarrow Ce^{3+}$ and $O^{2-} \rightarrow Ce^{4+}$ charge transfers, respectively [21]. For the CuCe-Z catalyst, the band at 209 nm can be related to the $O^{2-} \rightarrow Cu^+/Cu^{2+}$ and $O^{2-} \rightarrow Ce^{3+}$ charge transfers. However, UV–vis cannot distinguish between each of them, probably due to the electron interaction between Cu^{2+} and Ce^{3+} ions, leading to the band at 217 nm (assigned to $O^{2-} \rightarrow Ce^{3+}$ charge transfer) shifting to low wavelengths [22]. These results are consistent with those of XPS. A new band appearing at 371 nm is ascribed to Cu^{2+}–O^{2-}–Cu^{2+} charge transfer of highly dispersed lattice and surface Cu^{2+} species [21]. The reduction of visible light absorption (742 nm), together with a new band at 371 nm after the cerium addition (CuCe-Z), confirms the enhancement of copper dispersion.

3.5. Reduction behavior, oxygen and carbon monoxide storage capability

The redox behavior of the Cu-Z, Ce-Z and CuCe-Z catalysts has been investigated by H_2-TPR. As shown in Fig. 5 and Table 4, three reduction peaks have been identified in the Cu-Z catalyst: the β-peak (228 °C) is generally proposed as a result of the reduction of copper clusters dispersed on the ZSM-5 support; the γ-peak (286 °C) quite intense, is generally proposed as a result of the copper oxide minicrystals adhering to the external surface of zeolite crystallites; whereas the ζ-peak (371 °C) quite weak, is ascribed to the reduction of Cu^{2+} ions of the bulk-type CuO particles. Similarly for the Ce-Z catalyst, the δ- (299 °C), ε- (397 °C) and η-peaks (556 °C) are assigned to the reduction of cerium oxide clusters, minicrystals and the bulk ceria particles, respectively.

Table 4
Redox properties, carbon monoxide and oxygen storage capacities of Cu-Z, Ce-Z and CuCe-Z catalysts.

Sample	The center of redox peak (°C)							OSC (μmol [O] g^{-1})	CSC (μmol [CO] g^{-1})
	α	β	γ	δ	ε	ζ	η		
Cu-Z	/	228	286	/	/	371	/	16.2	6.2
Ce-Z	/	/	/	299	397	/	556	33.5	0.8
CuCe-Z	197	227	262	290	339	389	447	91.6	6.5

When both the copper and cerium are loaded on ZSM-5 (CuCe-Z), the β-, γ-, δ- and ε-peaks shift evidently to low regions, while the β- and δ-peaks narrow and increase in intensity because the copper and cerium disperse well (Fig. 5). Considering the surface enrichment of copper detected by XPS, it is reasonable to imagine that the copper clusters seem to preferentially cover the cerium phase. These species in proximity to the cerium phase are more easily reduced by hydrogen than that on the pure ZSM-5 support, since the presence of cerium increases oxygen migration. Moreover, part of copper species has been incorporated into the vacant sites of cerium oxides to form coordinated surface structure with the capping oxygen [23], corresponding to the α-peak (197 °C). This copper species, present as substitutional defects in the ceria lattice, can probably migrate outside the cerium oxide network to become highly dispersed copper ions, which are easily reducible for the intimate contact with ceria [24].

The OSC of catalysts is evaluated by the O_2 pulsing technique at 200 °C. It can be seen from Table 4 that the OSC values of the Cu-Z and Ce-Z are 16.2 and 33.5 μmol [O] g^{-1}, respectively. Compared with Cu-Z and Ce-Z, the remarkable enhancement of OSC can be observed for the CuCe-Z, which indicates that the combination of copper and cerium forms composite oxides over the ZSM-5 support, which strongly favors the creation of oxygen vacancies and therefore promotes the migration ability of oxygen ions [25]. CO chemisorption uptakes are also displayed in Table 4. Almost no carbon monoxide is consumed on the Ce-Z, whereas the Cu-Z and CuCe-Z catalysts present similar values of 6.2 and 6.5 μmol [CO] g^{-1}, respectively, indicating that the CO molecules tend to be chemisorbed on the copper sites of the Cu-Z and CuCe-Z catalysts.

3.6. DRIFT analysis

Because of the excellent activity of CuCe-Z for the CO conversion, the formation of surface species on CuCe-Z is probed by in situ DRIFT spectroscopy. At 100 °C, the sample is exposed to a flow of CO + O_2/He, and then DRIFT spectra are recorded in succession at 2-min intervals until the spectrum is stable. As shown in Fig. 6, the adsorption bands at 1036, 1597 and 1665 cm^{-1} are assigned to the bidentate carbonates, while the bands at 1084, 1319, 1482 and 1529 cm^{-1} correspond to monodentate carbonates, reflecting the intense C=O stretching bands [26]. The formation of these carbonate species involves adsorption of CO molecules on the coordinative unsaturated Lewis acid-based pair sites [27]. Moreover, the band in the spectra of non-coordinated carbonates is observed at 1430 cm^{-1}. At higher wavenumbers, the bands at 2112 and 2172 cm^{-1} are related to the C–O stretching mode of Cu^{n+}–CO complexes [28,29]. The intensities of bands at 2112 and 2172 cm^{-1} are significantly higher than those of the bands at 1036, 1084, 1319, 1482, 1529, 1597 and 1665 cm^{-1}, indicating that CO molecules are easier adsorbed to form Cu^{n+}–CO complexes than carbonates. The gaseous CO_2 band signals at 2335 and 2361 cm^{-1} can be also tracked, which is originated from the oxidation of Cu^{n+}–CO and carbonate species. Hence it can be convinced that carbon monoxide is weakly catalyzed to form carbon dioxide at low temperatures. When the spectra are measured stepwise to higher temperatures (150–300 °C), two broad peaks in the range of 1200–2000 cm^{-1} are observed. Although they are possibly composed of many carbon-oxygen complexes, both two peak centers located at 1529 and 1669 cm^{-1}, corresponding to the monodentate and bidentate carbonates, respectively, are of great dominance. With the temperature increasing, the signals of Cu^{n+}-CO complexes (2112 and 2172 cm^{-1}) weaken rapidly but vanish at 300 °C. By contrast, the signals of gaseous CO_2 (2335 and 2361 cm^{-1}), monodentate (1529 cm^{-1}) and bidentate (1669 cm^{-1}) carbonates intensify monotonously with temperature. These behaviors can be explained by the fact that the Cu^{n+}–CO complexes have a lower thermal stability than that of monodentate and bidentate carbonates. In this case, the Cu^{n+}–CO complexes are first decomposed to CO_2 at temperatures ≥150 °C, followed by decomposition of carbonates.

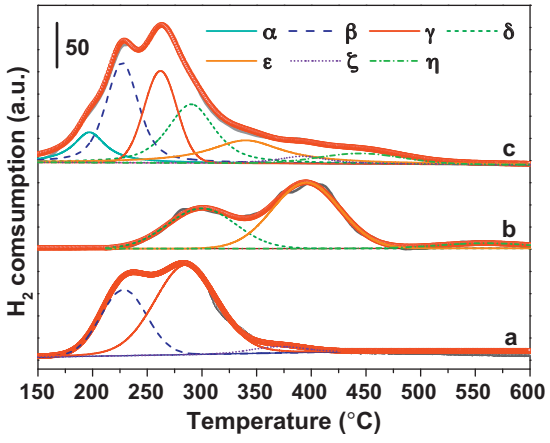

Fig. 5. H_2-TPR profiles of Cu-Z (a), Ce-Z (b) and CuCe-Z (c) catalysts. Crude line: original data; Smooth line: fitting line. Weight of catalyst: 100 mg; Pretreatment: He at 300 °C for 1 h; Measurement conditions: 5 vol.% H_2 (50 mL/min) with Ar balance, heating rate 10 °C/min from 50 to 600 °C.

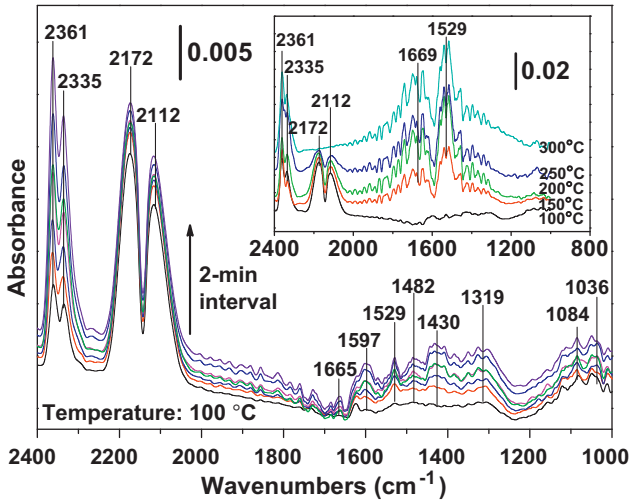

Fig. 6. DRIFT spectra for co-adsorbed CO/O_2 on the CuCe-Z catalyst after exposure to 2.5 vol.% CO + 20 vol.% O_2/He at 100–300 °C. The reaction gas mixture (2.5 vol.% CO, 20 vol.% O_2, He balance) was fed to the sample at a total flow rate of 30 mL min^{-1}.

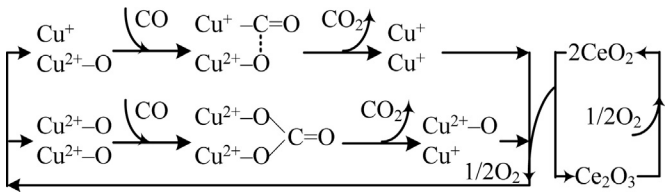

Fig. 7. The proposed reaction pathways for CO oxidation over the CuCe-Z catalyst.

3.7. Proposed reaction pathway

Based on the above results, we deduce that the CO catalytic combustion over metal-based ZSM-5 catalysts follows the Mars-van Krevelen mechanism, and the proposed reaction pathway of CO oxidation is displayed in Fig. 7. The adsorption of CO on the catalyst surface is considered to be the crucial step for CO catalytic combustion. The CO molecules are chemisorbed on the copper sites rather than cerium sites since CSC results confirm that almost no CO molecules are chemisorbed on the Ce-Z. Copper species exist in copper ions, amorphous copper clusters, copper oxide minicrystals, and bulk-type CuO particles. For the CuCe-Z catalyst, the DRIFT study suggests that CO is preferentially adsorbed on Cu^+ ions to yield Cu^+–CO complexes because the intensities of bands related to the Cu^{n+}–CO complexes are significantly higher than those related to the carbonates. The adsorbed CO interacts with an oxygen atom bonded to a neighboring Cu^{2+} atom in a strongly exothermic reaction, forming the gaseous CO_2 release, and then the reduced-state Cu^+ is obtained. CO is secondly adsorbed on the surface activated oxygen of Cu^{2+} sites to produce monodentate and bidentate carbonates. Further decomposition of carbonates to CO_2 involves the uptake of the activated oxygen and simultaneous reduction of Cu^{2+} to Cu^+. In addition, the H_2-TPR characterization also testifies that the copper ions are more reducible than the copper clusters and minicrystals, which are in consistent with the DRIFT results. The OSC analysis validates that the combination of copper and cerium strongly favors the creation of oxygen vacancies and therefore promotes the migration ability of oxygen ions. Due to the oxygen storage of cerium oxides, the Ce^{4+} cation at the neighboring site of the reduced Cu^+ site can supply additional oxygen atoms from the catalyst lattice through the reduction of Ce^{4+} to Ce^{3+}, while Cu^+ is simultaneously oxidized to Cu^{2+}. Ce^{3+} (with oxygen vacancies) may be re-oxidized directly by gas phase oxygen or by oxygen diffusion though the bulk of the catalyst. During each catalytic cycle, the redox electron transfer between copper and cerium follows the equilibrium ($Cu^+ + Ce^{4+} \leftrightarrow Cu^{2+} + Ce^{3+}$), as described in the XPS analysis. After another surface active oxygen species is formed, CO can be re-adsorbed and interact with the active oxygen atom, in which case the catalytic cycle is maintained.

The TPO process has confirmed that the Ce-Z catalyst is inactive for the CO combustion while the Cu-Z and CuCe-Z exhibit a good performance in the temperature range of 50–300 °C. The low activity of Ce-Z can be ascribed to the weak adsorption of CO. CO has a small dipole moment and is only a weak donor. Thus, a strong bonding of CO to metal oxide surfaces depends upon the back donation of electrons from the surface cations into the anti-bonding π-orbital [30], which are generally provided by d-orbital of the metal. The outer shell electron distributions of Cu^+ and Cu^{2+} are 3d10 and 3d9, respectively, and the d-orbitals are completely or nearly full of electrons. Hence both Cu^+ and Cu^{2+} are prone to establish strong bonding to CO, especially the former. In this case, the species of Cu^+ are the active sites of the Cu-Z and CuCe-Z catalysts for the CO catalytic combustion. With respect to the Ce-Z catalyst, however, the Ce^{3+} and Ce^{4+}, with the outer shell electron distributions of 4f1 and 5S2 4d10 5P6, respectively, are difficult to offer the electrons from d-orbitals to the anti-bonding π-orbitals, and the affinity between cerium and CO is consequently weak.

The CuCe-Z catalyst exhibits higher activity than that of the Cu-Z catalyst. One possible reason may be that the cerium addition into Cu-Z promotes part of the Cu^+ oxidized to Cu^{2+} that are incorporated into cerium oxides. These Cu^{2+} formed are more reducible than the copper clusters, minicrystals and bulk-type CuO particles. The activity enhancement of the CuCe-Z is probably also attributable to the redox couple Ce^{4+}/Ce^{3+}, which not only improves the oxygen storage capacity but facilitates oxygen transport through surface/bulk diffusion so that more oxygen is available for the CO combustion [31]. When the reaction temperature is high enough, the active site becomes a hot spot of exothermic reaction, due to the fast mass transfer on the catalyst surface. The reaction can be accelerated and subsisted by the heat generation from itself, thus leading to form a marked hysteresis. After the surface reaction rate exceeds the diffusion rate (in gas phase or in the porous support) of reactants, the CO oxidation reaction becomes autocatalytic combustion and even the self-sustained combustion at room temperature for the CuCe-Z catalyst.

4. Conclusions

The catalytic combustion of carbon monoxide in excess oxygen has been studied over the Cu-Z, Ce-Z and CuCe-Z catalysts. The results show that the activity for the CO combustion follows the order: CuCe-Z > Cu-Z > Ce-Z as indicated by lower T_i, T_{io}, T_{ex} and higher ΔT. Due to its poor capacity of CO adsorption, the Ce-Z catalyst is inactive at 50–300 °C. Compared with the Cu-Z, the enhancement of activity over the CuCe-Z catalyst is due to the formation of Cu^{2+} ions incorporated into cerium oxides, which are more reducible than the copper clusters, minicrystals and bulk CuO particles. On the other hand, the redox couple Ce^{4+}/Ce^{3+} formed facilitates oxygen transport. In this case, the CO combustion can be accelerated with temperature elevation, leading to form a marked hysteresis and even a self-sustained combustion of CO.

Acknowledgments

This work is financially supported by the National Natural Science Found of China (No. 51206119, 91130028). The work is also supported by State Key Laboratory of Engines, Tianjin University (K2014-8).

References

[1] M. Arens, E. Worrell, J. Schleich, Energy 45 (2012) 786–797.
[2] S. Li, X.L. Wei, L.X. Yu, Fuel 90 (2011) 1350–1360.
[3] U.R. Pillai, S. Deevi, Appl. Catal. B: Environ. 64 (2006) 146–151.
[4] J. Lundgren, T. Ekbom, C. Hulteberg, M. Larsson, C.E. Grip, L. Nilsson, P. Tunå, Appl. Energy 112 (2013) 431–439.
[5] J.E. Abboud, N. Jiang, Z. Zhang, S. Roy, J.R. Gord, Combust. Flame 160 (2013) 1842–1847.
[6] S.A. Smyth, K.T. Christensen, D.C. Kyritsis, Proc. Combust. Inst. 32 (2009) 3035–3042.
[7] K. Bijjula, D.G. Vlachos, Proc. Combust. Inst. 33 (2011) 1801–1807.
[8] A. Scarpa, R. Pirone, G. Russo, D.G. Vlachos, Combust. Flame 156 (2009) 947–953.
[9] F. Bin, C. Song, G. Lv, J. Song, S. Wu, X. Li, Appl. Catal. B: Environ. 150–151 (2014) 532–543.
[10] E.A. Goldstein, R.E. Mitchell, Proc. Combust. Inst. (2011) 2803–2810.
[11] A. Vasile, V. Bratan, C. Hornoiu, M. Caldararu, N.I. Ionescu, T. Yuzhakova, Á. Rédey, Appl. Catal. B: Environ. 140–141 (2013) 25–31.
[12] P.A. Carlsson, M. Skoglundh, Appl. Catal. B: Environ. 101 (2011) 669–675.
[13] K. Arnby, J. Assiks, P. Carlsson, J. Catal. 233 (2005) 176–185.
[14] E.E. Iojoiu, B. Bassou, N. Guilhaume, Catal. Today 137 (2008) 103–109.
[15] T. Zhang, J. Liu, D. Wang, Z. Zhao, Y. Wei, K. Cheng, G. Jiang, A. Duan, Appl. Catal. B: Environ. 148–149 (2014) 520–531.
[16] M. Dükkancı, G. Gündüz, S. Yılmaz, Y.C. Yaman, R.V. Prikhod'ko, I.V. Stolyarova, Appl. Catal. B: Environ. 95 (2010) 270–278.

[17] M.L.M. Oliveira, C.M. Silva, R. Moreno-Tost, T.L. Farias, A. Jiménez-López, E. Rodríguez-Castellón, Appl. Catal. B: Environ. 88 (2009) 420–429.
[18] L. Katta, P. Sudarsanam, G. Thrimurthulu, B.M. Reddy, Appl. Catal. B: Environ. 101 (2010) 101–108.
[19] X. Liao, W. Chu, X. Dai, V. Pitchon, Appl. Catal. A: Gen. 449 (2012) 131–138.
[20] C. Liang, X. Li, Z. Qu, M. Tade, S. Liu, Appl. Surf. Sci. 258 (2012) 3738–3743.
[21] V.D. Araújo, J.D.A. Bellido, M.I.B. Bernardi, J.M. Assaf, E.M. Assaf, Int. J. Hydrogen Energy 37 (2012) 5498–5507.
[22] L. Liu, Z. Yao, B. Liu, L. Dong, J. Catal. 275 (2010) 45–60.
[23] G. Deo, I.E. Wachs, J. Catal. 146 (1994) 323–334.
[24] E. Moretti, Loretta Storaro, Aldo Talon, Appl. Catal. B: Environ. 102 (2011) 627–637.
[25] K. Sun, W. Lu, M. Wang, X. Xu, Appl. Catal. A: Gen. 268 (2004) 107–113.
[26] C.W. Tang, L.C. Hsu, S.W. Yu, C.B. Wang, S.H. Chien, Vib. Spectrosc. 65 (2013) 110–115.
[27] I. Tankov, W.H. Cassinelli, J.M.C. Bueno, K. Arishtirova, S. Damyanova, Appl. Surf. Sci. 259 (2012) 831–839.
[28] C.H. Tseng, T.C.K. Yang, H.E. Wu, H.C. Chiang, J. Hazard. Mater. 166 (2009) 686–694.
[29] H. Zhou, Z. Huang, C. Sun, F. Qin, D. Xiong, W. Shen, H. Xu, Appl. Catal. B: Environ. 125 (2012) 492–498.
[30] M. Kang, M.W. Song, C.H. Lee, Appl. Catal. A: Gen. 251 (2003) 143–156.
[31] D. Martin, D. Duprez, J. Phys. Chem. 100 (1996) 9429–9438.